

Plasmonic sensor realized on a metal-insulator-metal waveguide configuration for refractive index detection

Muhammad Ali Butt*

Warsaw University of Technology, Institute of Microelectronics and Optoelectronics, Koszykowa 75, 00-662 Warszawa, Poland

Received October 21, 2021; accepted February 22, 2022; published March 31, 2022

Abstract—In this work, a plasmonic sensor established on a metal-insulator-metal waveguide configuration is proposed and numerically investigated for biosensing applications. The spectral and sensing characteristics of the device are examined via the two-dimensional finite element method. Sensitivity (S_{bulk}) and figure of merit (FOM) are two important parameters that are considered to determine the device performance. The S_{bulk} of the device is considered as a ratio between the change in resonance wavelength and a change in the ambient refractive index. Whereas FOM is the ratio of S_{bulk} to full width at half maximum. The S_{bulk} and FOM offered by the device are $\sim 825.7\text{nm}/\text{RIU}$ and ~ 13.14 , respectively. This work can provide a guideline for the realization of highly sensitive plasmonic sensing devices.

Plasmonic waveguides (abbreviated as WGs) such as a metal-insulator-metal (abbreviated as MIM) configuration is a breakthrough in the realization of compact plasmonic devices [1]. The WG structure is formed by enclosing an insulator (can be air, $n=1.0$) between two metal claddings. The uncomplicated design and capability of these WGs to restrict the light at the subwavelength level are the key attributes of this WG system. Surface plasmon polariton (SPP) induced as the surface electromagnetic waves travel along the metal-dielectric boundary is created by the incident photons coupled to the free electrons. SPP waves overcome the diffraction limit of light and provide the optical confinement within sub-wavelength order. It is possible to realize distinct attractive devices established on these WG structures such as a splitter [2–3], polarizer [4], laser source [5], multiplexer/demultiplexer [6], filter [7] and sensor [8], among others.

Over the past few years, several highly sensitive plasmonic sensing devices established on the MIM WG structure have been proposed for biochemical, gas, temperature and pressure sensing applications [9–13]. In this work, we have proposed a simple configuration of a plasmonic sensing device established on MIM WG. The cavity is formed by combining cross and square shapes known as square-cross-cavity (abbreviated as SCC). Figure 1 shows the 2D graphical illustration of the anticipated sensing device. The sensor design is composed of gold (Au) which is a biocompatible material, and the dielectric material which is considered as water ($n=1.33$) is filled in the SCC and bus WG. The SCC is side coupled to a straight bus WG of width W which is

preserved at 50nm throughout the paper. The gap between the bus WG and the SCC is symbolized as g . The side length of the square and cross is represented as L and $L+L_1$, respectively. The width of the cross is symbolised as W_1 which is maintained at $2W$, i.e., 100 nm throughout the paper. The relative dielectric constant of Au is described by the Drude-Lorentz dispersion model [14]:

$$\varepsilon = \varepsilon_{\infty} - \frac{\omega_p^2}{\omega^2 + j\omega\gamma},$$

where $\varepsilon_{\infty} = 9.0685$, $\omega_p = 135.44 \cdot 10^{14} \text{rad/s}$ and $\gamma = 1.15 \cdot 10^{14} \text{rad/s}$. The spectral characteristics and sensing performance are optimized by varying the structural variables of the device via the 2D finite element method (FEM). The fundamental mode that MIM WG endures is an even mode with a TM-polarization. Consequently, an SPP mode is excited, which propagates along the metal-dielectric boundary and couples to the SCC when the resonance condition is met.

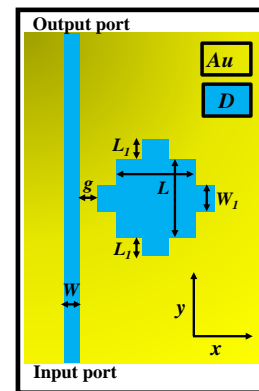


Fig. 1. Graphical illustration of a plasmonic sensor established on MIM WG structure.

In the first step, the transmission spectrum of the device is examined for the variation in L and other structural variables such as W , W_1 , L_1 and g are maintained at 50nm, 100nm, 200nm, and 20nm, respectively. The parametric sweep function is used to vary the input wavelength of light ranges between 950nm and 1450nm. The transmission is determined by using the following equation:

$$\text{Transmission} = P_{\text{out}}/P_{\text{in}},$$

* E-mail: ali.butt@pw.edu.pl

where P_{out} and P_{in} are the power at the output port and the power at the input port, respectively. As L varies from 300nm to 400nm, the resonance dip (λ_{dip}) performs a redshift due to an increase in the effective length of the SCC as demonstrated in Fig. 2. Therefore, we can choose the operational wavelength region by simply varying the length of the SCC.

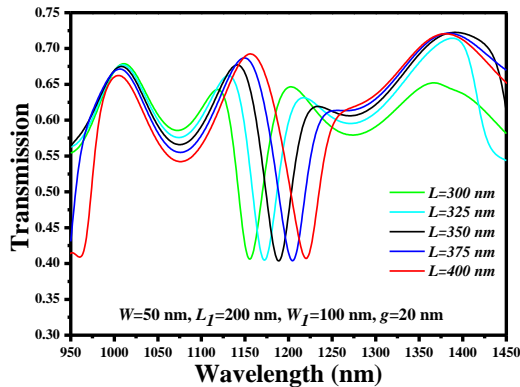


Fig. 2. Transmission spectrum versus variation in L .

In the next step, the influence of L_I on the transmission spectrum is examined by keeping L , W , W_I and g at 350nm, 50nm, 100nm, and 20nm, respectively. It is well noted that λ_{dip} executes a redshift as L_I surges from 160 nm to 220 nm as shown in Fig. 3. However, the shift in λ_{dip} is much bigger than the one obtained by varying L . At the optimized value of $L_I=180$ nm, λ_{dip} is strong and has a narrow full width at half maximum (FWHM=62.84 nm) which can lead to be a better figure of merit of the sensor.

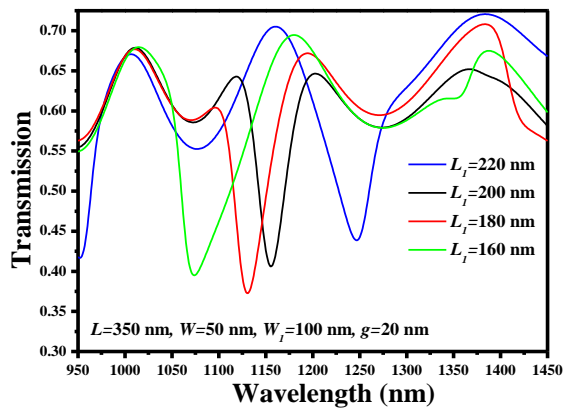


Fig. 3. Transmission spectrum versus variation in L_I .

The coupling gap (g) between the bus WG and the SCC is a vital factor to be considered while designing the plasmonic sensor. It should be optimized to obtain a strong coupling of the electromagnetic wave from the bus WG to the SCC. The transmission spectrum of the anticipated device is plotted by varying g from 10nm to 30nm with an interval of 5nm. The other structural parameters such as W , W_I , L and L_I are maintained at 50nm, 100nm, 350nm, and 180nm, respectively. From the

Fig. 4, it is evident that as g reduces to 10nm, the coupling power increases resulting in the strong λ_{dip} .

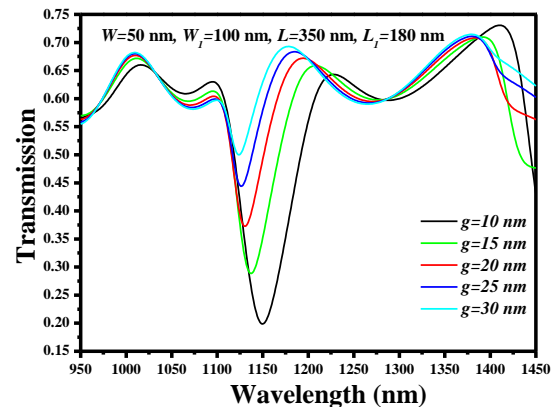


Fig. 4. Transmission spectrum versus variation in g .

The normalized H-field distribution at $\lambda=1150$ nm and $\lambda=1230$ nm is plotted for the optimized geometric parameters ($W=50$ nm, $W_I=100$ nm, $L=350$ nm, $L_I=180$ nm and $g=10$ nm) as shown in Fig. 5a and Fig. 5b, respectively. It can be noticed that when the resonance condition is satisfied, the SPP mode is restricted in the SCC creating a sharp dip in the transmission spectrum.

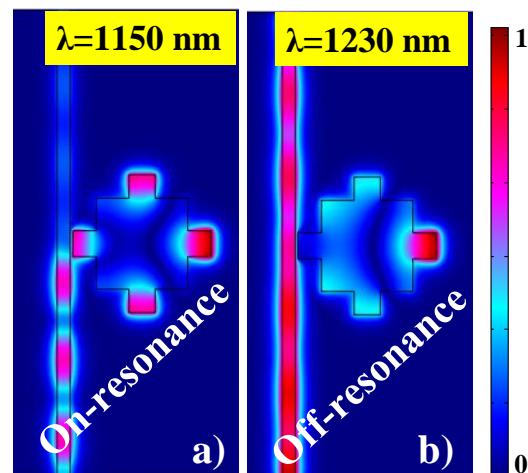


Fig. 5. Normalized H-field mapping at: a) 1150 nm, b) 1230 nm.

After adjusting the structural variables of the device, the transmission spectrum of the sensor is plotted concerning the variation in the surrounding refractive index (RI) as shown in Fig. 6a. The selected RI lies in the range of 1.33 to 1.38, which corresponds to the RI range of the biochemical analytes. The λ_{dip} presents a redshift as the RI of the medium upsurges, however, the value of shift in λ_{dip} is dependent on the sensitivity offered by the device.

SPP waves are very sensitive to fluctuations in the adjacent RI. A minor shift in the RI can be acquired by evaluating the variations in one of the features of the light joined to the SP wave, for instance, a shift in the resonance wavelength (λ_{res}), intensity, or phase.

Generally, the operational mechanism of the ring resonator is created on the wavelength examination process, which requires the evaluation of a swing in λ_{res} concerning the variation in the RI of the surrounding medium. The sensitivity (S_{bulk}) of the anticipated device can be calculated by means of the resulting expression [15]:

$$S_{bulk} = \Delta\lambda_{dip} / \Delta n,$$

where $\Delta\lambda_{dip}$ and Δn is the shift in λ_{res} and the shift in the RI of the adjacent medium, respectively. The λ_{res} of the device is plotted for the RI range of 1.33 to 1.38 as shown in Fig. 6b, which follows a linear trend. The estimated S_{bulk} is ~ 825.7 nm/RIU is obtained, which is much higher than several previous works [16-19]. The figure of merit (FOM) is an additional factor to assess the performance of the device and can be determined by utilizing the following expression:

$$FOM = S_{bulk} / FWHM,$$

where S_{bulk} and FWHM is the sensitivity and full width at half maximum, respectively. The FOM of the optimized device is ~ 13.14 .

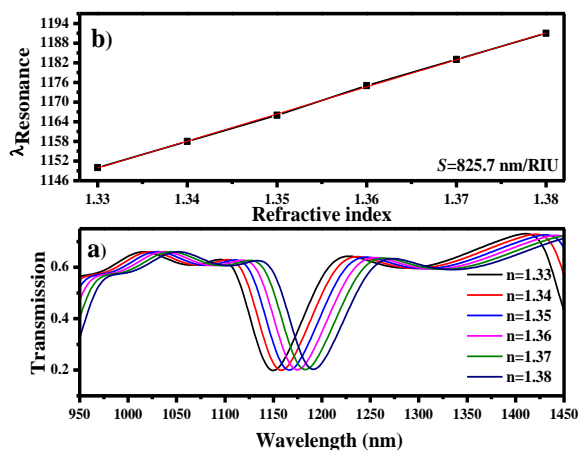


Fig. 6. Spectral characteristics of the sensor, a) Transmission spectrum for the RI range of 1.33-1.38, b) resonance wavelength shift for the RI range of 1.33-1.38.

In conclusion, we presented a plasmonic sensor device established on the MIM WG configuration for biosensing application. The numerical study is conducted via a 2D finite element method using COMSOL Multiphysics software. The sensitivity and FOM of the device are ~ 825.7 nm/RIU and ~ 13.14 , respectively, which is obtained by optimizing the structural variables of the device. We consider the investigation conducted in this work to be valuable for the apprehension of sensitive plasmonic sensing devices.

The research is co-financed by the Foundation for Polish Science from the European Regional Development Fund within the project POIR.04.04.00-00-14D6/18 "Hybrid sensor platforms for integrated photonic systems based on ceramic and polymer materials (HYPHa)" (TEAM-NET program).

References

- [1] N.L. Kazanskiy, S.N. Khonina, M.A. Butt, Physica E: Low-dimensional systems and Nanostructures **117**, 113798 (2020).
- [2] D. Xiang, W. Li, J. Modern Opt. **61**, 222 (2014).
- [3] M.A. Butt, S.N. Khonina, N.L. Kazanskiy, Laser Physics **30**, 016201 (2020).
- [4] J. Park, S. Lee, B. Lee, IEEE J. Quant. Electr. **46**, 1577 (2010).
- [5] M.T. Hill, M. Marell, E.S.P. Leong, B. Smalbrugge, Y. Zhu, M. Sun, P.J.V. Veldhoven, E.J. Geluk, F. Karouta, Y-S. Oei, R. Notzel, C-Z. Ning, M.K. Smit, Opt. Expr. **17**, 11107 (2009).
- [6] A. Udipi, S.K. Madhava, Plasmonics **16**, 1685 (2021).
- [7] Y-F.C. Chau, C-T.C. Chao, H-P. Chiang, Results in Phys. **17**, 103116 (2020).
- [8] H. Bahri, S. Mouetsi, A. Hocini, H.B. Salah, Opt. Quant. Electron. **53**, 332 (2021).
- [9] S.N. Khonina, N.L. Kazanskiy, M.A. Butt, A. Kazmierczak, R. Piramidowicz, Opt. Expr. **29**, 16584 (2021).
- [10] M.A. Butt, S.N. Khonina, N.L. Kazanskiy, Fiber and Integrated Optics **40**, 14 (2021).
- [11] M.A. Butt, A. Kazmierczak, N.L. Kazanskiy, S.N. Khonina, Electronics **10**, 1419 (2021).
- [12] N.L. Kazanskiy, S.N. Khonina, M.A. Butt, A. Kazmierczak, R. Piramidowicz, Nanomaterials **11**, 2551 (2021).
- [13] I. Tathif, A.A. Yaseer, K.S. Rashid, R.H. Sagor, Opt. Expr. **29**, 32365 (2021).
- [14] P.D. Sia, Nanoscale Syst. Math. Model. Theory Appl. **3**, 1 (2014).
- [15] M.A. Butt, N.L. Kazanskiy, Opt. Applicata **LI**, 109 (2021).
- [16] S. Khani, M. Hayati, Superlattices and Microstructures **156**, 106970 (2021).
- [17] F. Chen, J. Li, Modern Physics Letters B **33**, 1950017 (2019).
- [18] M. Rahmatiyar, M. Danaie, M. Afsahi, Opt. Quant. Electr. **52**, 153 (2020).
- [19] M.A. Butt, S.N. Khonina, N.L. Kazanskiy, Laser Physics Letters **16**, 126201 (2019).